Chemical Science

ROYAL SOCIETY OF CHEMISTRY

EDGE ARTICLE

View Article Online
View Journal | View Issue

Cite this: *Chem. Sci.*, 2023, **14**, 10347

All publication charges for this article have been paid for by the Royal Society of Chemistry

Received 8th June 2023
Accepted 31st August 2023

DOI: 10.1039/d3sc02946h

rsc.li/chemical-science

Mixing cage cations in 2D metal-halide ferroelectrics enhances the ferro-pyro-phototronic effect for self-driven photopyroelectric detection†

Yu Ma,[ab] Wenjing Li,[ab] Yi Liu,[a] Wuqian Guo,[ab] Haojie Xu,[ab] Shiguo Han,[a] Liwei Tang,[a] Qingshun Fan,[ab] Junhua Luo [a] and Zhihua Sun *[a]

The ferro-pyro-phototronic (FPP) effect, coupling photoexcited pyroelectricity and photovoltaics, paves an effective way to modulate charge-carrier behavior of optoelectronic devices. However, reports of promising FPP-active systems remain quite scarce due to a lack of knowledge on the coupling mechanism. Here, we have successfully enhanced the FPP effect in a series of ferroelectrics, $BA_2Cs_{1-x}MA_xPb_2Br_7$ (BA = butylammonium, MA = methylammonium, $0 \le x \le 0.34$), rationally assembled by mixing cage cations into 2D metal-halide perovskites. Strikingly, chemical alloying of Cs^+/MA^+ cations leads to the reduction of exciton binding energy, as verified by the $x = 0.34$ component; this facilitates exciton dissociation into free charge-carriers and boosts photo-activities. The crystal detector thus displays enhanced FPP current at zero bias, almost more than 10 times higher than that of the $x = 0$ prototype. As an innovative study on the FPP effect, this work affords new insight into the fundamental principle of ferroelectrics and creates a new strategy for self-driven photodetection.

Introduction

The ferro-pyro-phototronic (FPP) effect in ferroelectrics, coupling photovoltaics and photoexcited pyroelectricity, has emerged as an effective pathway to modulate charge-carrier behaviors of optoelectronic devices.[1] This unique light–matter interaction allows both stable photovoltaic current and instantaneous pyroelectric current; the former stems from the space electric field caused by electric polarization, while the latter relates to the redistribution of thermally induced pyroelectric charges in the polar direction.[2] In self-driven detectors, current transport closely relates to photogenerated potential, while the instantaneous thermoelectric potential caused by thermal stimulation can be utilized to modulate the transport properties of charge carriers, thereby achieving an enhancement in the device performance.[3] To date, existing investigations on the FPP effect have mainly focused on inorganic photoactive ferroelectric materials, including $BaTiO_3$, $BiFeO_3$, *etc.*[4] However, most of these inorganic materials possess a wide bandgap, weak light absorption and carrier transportation, which greatly limit their further application in photosensitive devices. Hence, it is of great significance but challenging to exploit new FPP-active candidate systems toward efficient self-driven photodetection.

Two-dimensional (2D) metal halide ferroelectrics with the formula $(A')_2A_{n-1}M_nX_{3n+1}$ (where A' is a spacer cation, A is a cage cation, M is a metal, and X is a halide) hold promise for application in photoelectric devices, owing to their high phase stability, natural quantum-well effect, and directional charge transport.[5] Structurally, dynamic A'- and A-site organic cations provide a driving force to induce ferroelectric order, and the rigid inorganic layer accounts for light absorption and carrier transport.[6] Specifically, the rational self-assembly of organic and inorganic components opens up new avenues for newly conceptual and intelligent optoelectric devices. For example, the FPP effect was actualized along the polar axis in (*n*-hexylammonium)$_2CsPb_2Br_7$, of which the directions can be switched reversibly by electric polarization; thin films based on $BA_2MA_3Pb_4Br_{13}$ allow for high-performance UV photoactivities through the FPP effect, as well as the broadband photodetection realized in (*p*-bromobenzylammonium)$_2$(ethylammonium)$_2$-Pb_3Br_{10}.[7] Although such 2D ferroelectrics are steadily booming as photoactive candidates, the study of their FPP properties is still in the initial stage due to a lack of knowledge on the coupling mechanism of photovoltaics and photoexcited pyroelectricity. Specifically, it remains a huge blank to modulate FPP activities of this 2D family through mixing A-site cage cations. In this context, it is highly urgent to develop 2D ferroelectric candidates with strong FPP effects to assemble smart optoelectronic devices.

[a]*State Key Laboratory of Structural Chemistry, Fujian Institute of Research on the Structure of Matter, Chinese Academy of Sciences Fuzhou, Fujian, 350002, China. E-mail: sunzhihua@fjirsm.ac.cn*

[b]*University of Chinese Academy of Sciences, Chinese Academy of Sciences, Beijing 100039, P. R. China*

† Electronic supplementary information (ESI) available. See DOI: https://doi.org/10.1039/d3sc02946h

In this work, we have successfully enhanced the FPP effect in a series of 2D ferroelectric crystals, $BA_2Cs_{1-x}MA_xPb_2Br_7$ ($0 \leq x \leq 0.34$), designed by mixing cage cations into metal-halide perovskites. Emphatically, the chemical alloying of Cs^+/MA^+ cations gives rise to the reduction of exciton binding energy, as verified by the $x = 0.34$ component. This facilitates exciton dissociation into free charge-carriers and boosts photoelectric properties of devices. As expected, a single-crystal detector of $BA_2Cs_{0.66}MA_{0.34}Pb_2Br_7$ shows enhanced FPP current at zero bias, being almost more than 10 times higher than that of the $x = 0$ prototype. Besides, crucial figures-of-merit including the maximum responsivity and detectivity of the $x = 0.34$ component are dramatically increased by an order of magnitude to 40 mA W^{-1} and 1.12×10^{12} Jones, respectively. To the best of our knowledge, this work should be the first to enhance FPP effects by mixing cage cations in 2D metal-halide ferroelectrics, which would establish a new strategy for actualizing self-driven photodetection.

Results and discussion

All the metal-halide perovskites of the $BA_2Cs_{1-x}MA_xPb_2Br_7$ family adopt a typical 2D bilayer structure composed of corner-sharing $PbBr_6$ octahedra, resembling that of $BA_2CsPb_2Br_7$.[8] A potential difference is that the Cs^+ cations situated in the perovskite cages are partially substituted by the organic MA^+ cation (Fig. 1a). The raw compounds of the $BA_2Cs_{1-x}MA_xPb_2Br_7$ family were prepared according to the chemical proportions ($x = 0$, 0.07, 0.21, 0.34), and the aqueous solution cooling method was utilized to grow single crystals (Fig. 1b). It should be noted that the concentration of MA^+ cations in the final crystals determined by elemental analysis may differ from that in the precursor. Hence, an elemental analyzer was employed to determine the detailed MA^+ cation fraction of the x value (Table S1†). Powder X-ray diffraction (XRD) measurements show that the chemical alloying of MA^+ cations exerts almost no obvious change on their crystal structures. As depicted in Fig. 1c, all the diffraction patterns of the doped sample are similar to those of the $BA_2CsPb_2Br_7$ prototype, indicating the coherence of their basic motifs. As the concentration of MA^+ cations increases, the main diffraction peaks move slightly towards a low-angle region (around 15°), suggesting that the replacement of the Cs^+ cation (~169 pm) by the larger MA^+ cation (~217 pm) results in lattice expansion.[9] This is further validated by the increasing unit cell parameters obtained by single-crystal diffraction at a higher MA^+ concentration (Table S2†).

Investigation of physical properties related to the ferroelectric phase transitions of the $BA_2Cs_{1-x}MA_xPb_2Br_7$ family is of particular importance. Primarily, differential scanning calorimetry (DSC) and dielectric measurements were utilized to

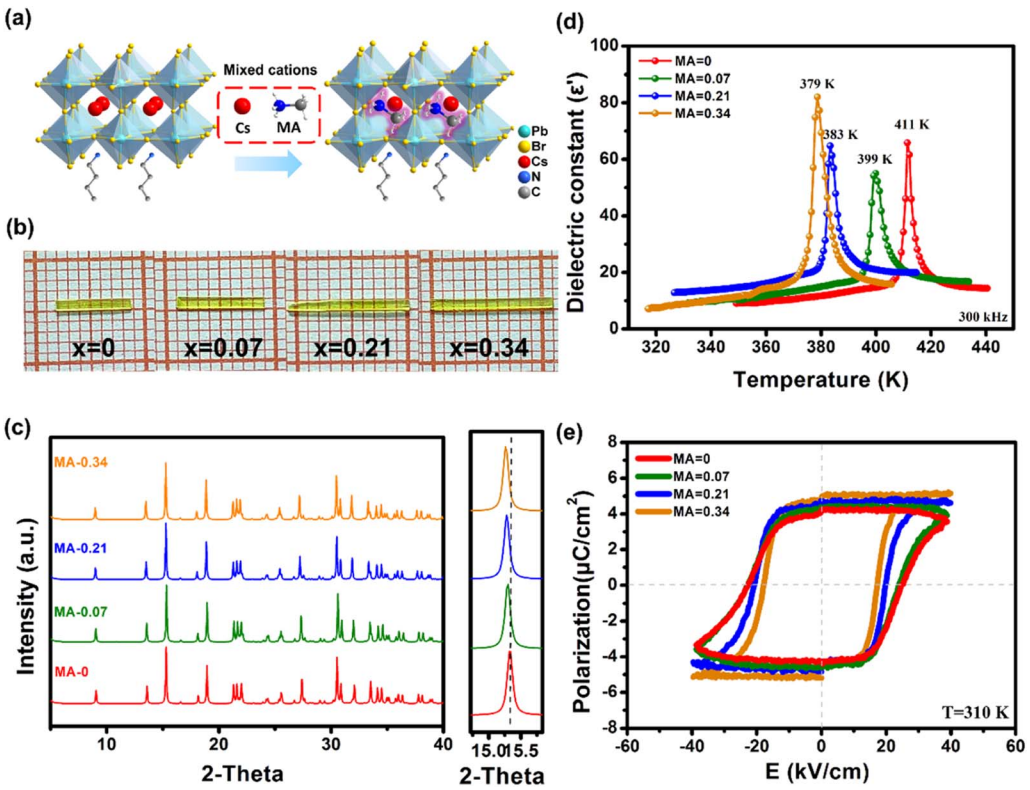

Fig. 1 Basic physical properties of $BA_2Cs_{1-x}MA_xPb_2Br_7$ crystals. (a) Diagram of mixing organic MA^+ cations into the perovskite cage of the prototype structure $BA_2CsPb_2Br_7$. (b) Photographs of pristine ($x = 0$) and derivatives of $BA_2Cs_{1-x}MA_xPb_2Br_7$ ($0 \leq x \leq 0.34$) crystals. (c) Powder XRD patterns of $BA_2Cs_{1-x}MA_xPb_2Br_7$ crystals. The enlarged 2θ range of XRD patterns shows the shift of diffraction peaks to lower angles with the increasing MA^+ cation concentrations. (d and e) Temperature-dependent dielectric measurements and P–E hysteresis loops of $BA_2Cs_{1-x}MA_xPb_2Br_7$, revealing the preservation of stable ferroelectricity.

confirm their phase transition behaviors. As depicted in Fig. S1,† the DSC curves of $BA_2Cs_{1-x}MA_xPb_2Br_7$ ($x = 0$, 0.07, 0.21, 0.34) show obvious endo/exothermic peaks in the heating/cooling runs. As the MA^+ cation ratio increases, the phase transition temperature (T_c) gradually decreases from 412 to 380 K. In addition, the sharp λ-peak anomalies can be clearly observed in temperature-dependent dielectric measurements (Fig. 1d). The peak temperatures of these sharp dielectric anomalies also decrease with the increasing MA^+ cation proportion, well consistent with the DSC results. Furthermore, polarization-electric field (P–E) hysteresis loop measurements reveal that the inherent ferroelectricity of the crystal remains stable upon addition of the mixed cage cations. The spontaneous polarization (P_s) values (~4.8 μC cm^{-2}) increase slightly (Fig. 1e), and the corresponding crystal breakdown voltage has an increased trend (Fig. S2†). Therefore, the superior ferroelectric properties of the $BA_2Cs_{1-x}MA_xPb_2Br_7$ family establish a solid foundation for achieving high-performance self-driven photoelectric responses.

The optical and semiconducting properties of materials are critical for optoelectronic applications. UV-visible absorption was performed to investigate the optical absorption of the $BA_2Cs_{1-x}MA_xPb_2Br_7$ family. Compared with the absorbance for $x = 0$, the $x = 0.34$ member has an absorption edge shifted to ~511 nm with the increasing MA^+ cation proportion (Fig. S3†). As a result, the corresponding bandgap values are modulated to a lower energy region (from 2.7 to 2.43 eV). Subsequently, photoelectric characteristics of the $BA_2Cs_{1-x}MA_xPb_2Br_7$ family were initially studied using lateral crystal-based devices under 405 nm laser irradiation. Under identical conditions (at 74 mW cm^{-2}), the alloying of MA^+ cations has greatly enhanced the photoactivity of crystal samples by at least tenfold. For instance, a maximum photocurrent of $x = 0.34$ can reach 600 μA cm^{-2}, exceeding that of $x = 0$, which is also 10^4 times higher than the dark current (Fig. S4†). Therefore, these excellent photoresponses achieved by the mixing cage cations inspire us to further investigate the potential photoelectric application of this 2D family.

Spontaneous electric polarization would create an ultrahigh built-in electrostatic field in ferroelectrics, which might facilitate the migration of photoexcited charge carriers and allow intriguing bulk photovoltaic effects.[10] In principle, light-induced pyroelectricity is closely associated with the variation of ferroelectric P_s, which leads to the compensating current, namely, pyroelectric current.[11] Therefore, the coexistence of ferroelectricity and photoelectric characteristic encourage us to investigate the FPP properties of the $BA_2Cs_{1-x}MA_xPb_2Br_7$ family. Single crystals of $x = 0.34$ were used as the representative to fabricate photoelectric devices (Fig. 2a), and the detailed photoelectric behaviors are shown in Fig. 2. The I–V curves measured at equal illumination power reveal that the bulk photovoltaic effect of $x = 0.34$ is superior to that of pristine $x = 0$ (the current plateau in Fig. 2b), thus affording promise for self-driven photodetection. Emphatically, the FPP behaviors are clearly observed and compared between the two analogues ($x = 0$ and $x = 0.34$), including pyroelectric and photovoltaic currents. For $x = 0$, the plateau current density of photovoltaics was found to be 0.6 μA cm^{-2} and the photo-pyroelectric peak current density was extremely small (~0.1 μA cm^{-2}). In contrast, the $x = 0.34$ member exhibits markedly different behaviors,

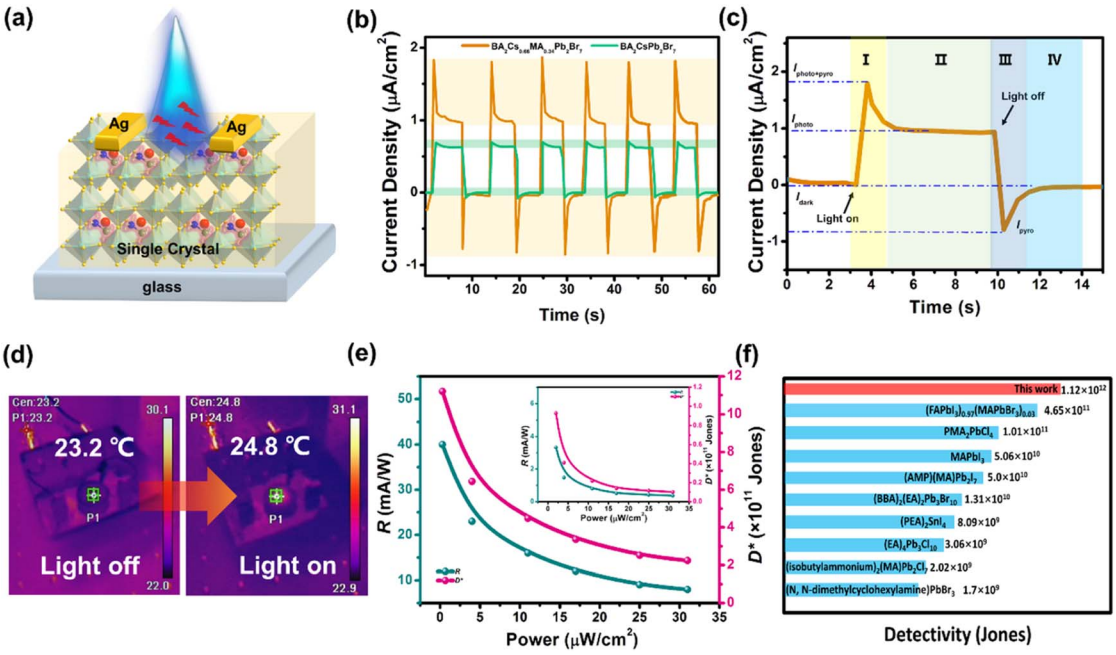

Fig. 2 Photopyroelectric properties of the $BA_2Cs_{1-x}MA_xPb_2Br_7$ family. (a) Diagram of a photopyroelectric device based on $x = 0.34$ crystals. (b) I–t curves of $x = 0.34$ and $x = 0$ members under periodical irradiation (405 nm, 32.17 mW cm^{-2}) without external bias. (c) One representative cycle of the current curve. (d) The identifiable temperature variation of the crystal surface. (e) Calculated R and D^* values of $x = 0.34$ as a function of power density. Inset: R and D^* values for $x = 0$. (f) Comparative D^* values of some known self-driven detectors based on hybrid perovskites.

such as the enhancement of photovoltaic plateau current density to 1 μA cm^{-2}. It is noteworthy that the peak currents associated with the FPP effect are dramatically improved by 10 times (Fig. 2b). We also measured under 450 nm light illumination, and there was also a significant FPP effect (Fig. S5†). These results indicate that the FPP effect has been significantly improved by chemical alloying of cage cations. As far as we know, this photopyroelectric current should be higher than that of the majority of known FPP-active materials, such as PMA_2PbCl_4, (*n*-hexylammonium)$_2CsPb_2Br_7$, *etc.*[7a,12] One representative cycle of the *I*–*t* curve with four photoactive stages is displayed in Fig. 2c. Initially, with light switching on, the combination of photovoltaics and photoexcited pyroelectricity affords strong photoactivities ($I_{pyro+photo}$, the I stage). When temperature remains constant under light illumination, pyroelectric current rapidly vanishes and only the plateau of photovoltaic current can be observed (I_{photo}, the II stage). Transient pyroelectric current (I_{pyro}) with a reversible direction emerges after turning off the light, caused by the variation of P_s (the III stage). Without illumination, the pyroelectric current disappears and the ultimate state returns to the dark conditions (the IV stage, Fig. S6†). The identifiable temperature fluctuation of crystals by light illumination with an intensity of ~32 mW cm^{-2} is measured to be 1.6 K from the surface mapping (Fig. 2d).

Photoactive properties of crystal-based devices under 405 nm laser irradiation at zero bias are depicted in Fig. 2e. As two key parameters to evaluate device capacity, both responsivity (*R*) and detectivity (*D**) are highly dependent on light intensities. However, performances of $x = 0.34$ are much superior to those of the $x = 0$ prototype, due to the enhanced FPP effect through the chemical mixing of cage cations. For $BA_2Cs_{0.66}MA_{0.34}Pb_2Br_7$, the maximum *R* and *D** values are calculated to be 40 mA W^{-1} and 1.12×10^{12} Jones, which are at least one order of magnitude higher than those of $BA_2CsPb_2Br_7$ ($R = 3.33$ mA W^{-1} and $D^* = 9.3 \times 10^{10}$ Jones, at 0.3 μW cm^{-2}). These two figures-of-merit exceed those of previously reported self-driven detectors based on hybrid perovskites (Fig. 2f).[13] Besides, the transient light-induced pyroelectric currents remain constant after ~10^3 cycles without any obvious fatigue, disclosing the notable photostability of our crystal-based device (Fig. S7†). The rise and fall response times of the device are 0.59 and 1.07 s, respectively (Fig. S8†). All these results confirm that the design strategy of mixing cage cations in 2D perovskite ferroelectrics is feasible to enhance the FPP effect and reveal that $BA_2Cs_{0.66}MA_{0.34}Pb_2Br_7$ might be a promising candidate for self-driven photopyroelectric detection.

To deeply understand the origin of the strong FPP effect in the $BA_2Cs_{1-x}MA_xPb_2Br_7$ family, we have performed the temperature-dependent photoluminescence (PL) spectral and space-charge-limited current (SCLC) measurements of $x = 0$ and 0.34 crystals, respectively.[14] As shown in Fig. 3a and b, the PL intensities decrease continuously with the increasing temperature from 77 to 300 K (Fig. S9†). Based on the Arrhenius plot,[15] the exciton binding energies for $x = 0$ and 0.34 are calculated to be 85.8 and 58.4 meV, respectively (Fig. 3c and d). This finding suggests that the binding energy of excitons is reduced upon alloying MA^+ cations; the excitons are more likely to dissociate into free charge carriers and enhance the photoelectric response.[16] In addition, the mixing of cage cations results in

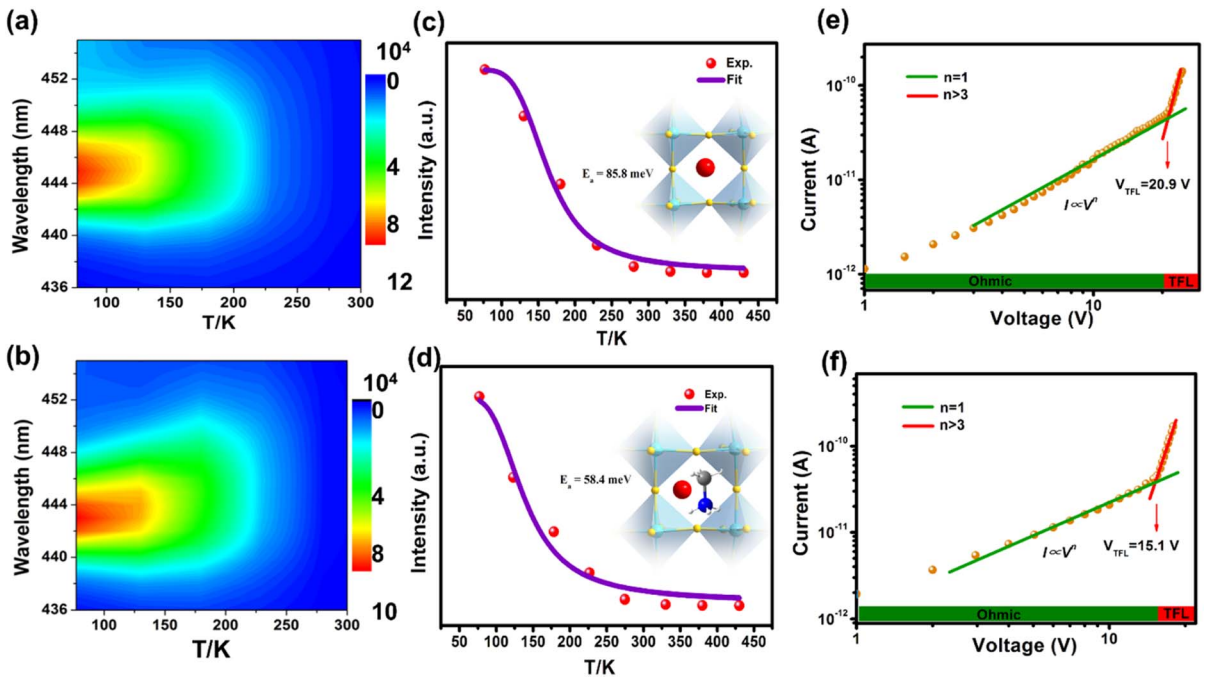

Fig. 3 Possible origin of strong FPP effects in the $BA_2Cs_{1-x}MA_xPb_2Br_7$ family. Contour plots of the temperature-dependent PL emission spectra of $x = 0$ (a) and $x = 0.34$ (b) in the temperature range of 77–300 K. Exciton binding energy determination of $x = 0$ (c) and $x = 0.34$ (d). The trap density measurements for single crystals of $x = 0$ (e) and $x = 0.34$ (f), respectively.

a decrease in trap-filled limit voltage from 20.9 V ($x = 0$) to 15.1 V ($x = 0.34$), and the trap densities are calculated to be 1.85 $\times 10^{11}$ cm^{-3} and 2.54 $\times 10^{10}$ cm^{-3}, respectively (Fig. 3e and f). Moreover, after applying the polarized field to the $x = 0.34$ device, the alignment of electric dipoles results in a stronger built-in electric field, which might enhance the FPP effect (Fig. S10†). Based on the above findings, it is proposed that the reduction of exciton binding energy and enhanced ferroelectric polarization account for a strong FPP effect in the $BA_2Cs_{1-x}MA_xPb_2Br_7$ family.

Conclusions

In summary, by mixing cage cations into 2D perovskite motifs, we have successfully obtained a series of ferroelectric crystals $BA_2Cs_{1-x}MA_xPb_2Br_7$ ($0 \leq x \leq 0.34$), which exhibit an enhanced FPP effect with an increasing proportion of organic cations. In particular, the chemical alloying of Cs^+/MA^+ cations leads to a reduction of exciton binding energy and increased polarization. This facilitates exciton dissociation into free charge-carriers and boosts photoelectric activities. As expected, a crystal-based detector of $x = 0.34$ shows enhanced FPP current at zero bias, which is almost more than 10 times higher than that of the $x = 0$ prototype. The corresponding maximum responsivity and detectivity are also one order of magnitude higher than those of $BA_2CsPb_2Br_7$. As an innovative study on the FPP effect, this work provides new insight into the fundamental principles of ferroelectrics and establishes a new strategy for assembling smart optoelectronic devices.

Data availability

The data supporting the findings of this study are available within the ESI.†

Author contributions

Yu Ma wrote the manuscript; Wenjing Li and Yi Liu performed the data analysis; Wuqian Guo and Haojie Xu performed the validation; Shiguo Han and Liwei Tang performed the data curation; Qingshun Fan performed the methodology; Junhua Luo and Zhihua Sun reviewed this article.

Conflicts of interest

There are no conflicts to declare.

Acknowledgements

This work was financially supported by NSFC (22125110, 22205233, 22193042, 21833010, 21921001 and U21A2069), the Key Research Program of Frontier Sciences of the Chinese Academy of Sciences (ZDBS-LY-SLH024), the Natural Science Foundation of Fujian Province (2023J01235), the National Key Research and Development Program of China (2019YFA0210402), and the China Postdoctoral Science Fund (2022TQ0337).

References

1 (*a*) I. Grinberg, D. V. West, M. Torres, G. Gou, D. M. Stein, L. Wu, G. Chen, E. M. Gallo, A. R. Akbashev, P. K. Davies, J. E. Spanier and A. M. Rappe, *Nature*, 2013, **503**, 509–512; (*b*) N. Ma, K. Zhang and Y. Yang, *Adv. Mater.*, 2017, **29**, 1703694; (*c*) T. Choi, S. Lee, Y. J. Choi, V. Kiryukhin and S. W. Cheong, *Science*, 2009, **324**, 63–66.

2 (*a*) L. You, F. Zheng, L. Fang, Y. Zhou, L. Z. Tan, Z. Zhang, G. Ma, D. Schmidt, A. Rusydi, L. Wang, L. Chang, A. M. Rappe and J. Wang, *Sci. Adv.*, 2018, **4**, 3438; (*b*) D. Kim, H. Han, J. H. Lee, J. W. Choi, J. C. Grossman, H. M. Jang and D. Kim, *Proc. Natl. Acad. Sci.*, 2018, **115**, 6566–6571.

3 (*a*) W. Peng, X. Wang, R. Yu, Y. Dai, H. Zou, A. C. Wang, Y. He and Z. L. Wang, *Adv. Mater.*, 2017, **29**, 1606698; (*b*) M. Kumar and H. Seo, *Adv. Mater.*, 2022, **34**, 2106881; (*c*) S. Han, Y. Ma, L. Hua, L. Tang, B. Wang, Z. Sun and J. Luo, *J. Am. Chem. Soc.*, 2022, **144**, 20315–20322.

4 (*a*) K. Zhao, B. Ouyang, C. R. Bowen and Y. Yang, *Nano Energy*, 2020, **77**, 105152; (*b*) K. Zhao, B. Ouyang and Y. Yang, *iScience*, 2018, **3**, 208; (*c*) M. Kumar, M. Patel, J. Kim and D. Lim, *Nanoscale*, 2017, **9**, 19201–19208; (*d*) R. Zhao, N. Ma, K. Song and Y. Yang, *Adv. Funct. Mater.*, 2020, **30**, 1906232.

5 (*a*) W. Guo, H. Xu, Y. Ma, Y. Liu, B. Wang, L. Tang, L. Hua, J. Luo and Z. Sun, *Adv. Funct. Mater.*, 2022, **32**, 2207854; (*b*) X. Li, F. Wu, Y. Yao, W. Wu, C. Ji, L. Li, Z. Sun, J. Luo and X. Liu, *J. Am. Chem. Soc.*, 2022, **144**, 14031–14036; (*c*) L. Lu, W. Weng, Y. Ma, Y. Liu, S. Han, X. Liu, H. Xu, W. Lin, Z. Sun and J. Luo, *Angew. Chem., Int. Ed.*, 2022, **61**, e202205030; (*d*) R. Ding, Y. Lyu, Z. Wu, F. Guo, W. F. Io, S.-Y. Pang, Y. Zhao, J. Mao, M.-C. Wong and J. Hao, *Adv. Mater.*, 2021, **33**, 2101263.

6 (*a*) Y. Ma, J. Wang, W. Guo, S. Han, J. Xu, Y. Liu, L. Lu, Z. Xie, J. Luo and Z. Sun, *Adv. Funct. Mater.*, 2021, **31**, 2103012; (*b*) Y. Liu, S. Han, J. Wang, Y. Ma, W. Guo, X.-Y. Huang, J.-H. Luo, M. Hong and Z. Sun, *J. Am. Chem. Soc.*, 2021, **143**, 2130–2137.

7 (*a*) Y. Liu, X. Pan, X. Liu, S. Han, J. Wang, L. Lu, H. Xu, Z. Sun and J. Luo, *Small*, 2022, **18**, 2106888; (*b*) L. Guo, Y. Qi, Z. Yang, L. Zhao, W. Zhang, X. Wang, H. Liu, G. Yan, S. Wang and C. Pan, *Nano Energy*, 2022, **102**, 107714; (*c*) L. Tang, W. Weng, H. Chen, L. Hua, W. Guo, Y. Liu, Y. Ma, Y. Chen, J. Luo and Z. Sun, *Adv. Funct. Mater.*, 2023, **33**, 2214858.

8 Z. Wu, C. Ji, L. Li, J. Kong, Z. Sun, S. Zhao, S. Wang, M. Hong and J. Luo, *Angew. Chem., Int. Ed.*, 2018, **57**, 8140–8143.

9 G. Sun, X. Liu, Z. Liu, D. Liu, F. Meng, Z. Li, L. Chu, W. Qiu, X. Peng, W. Xie, C. Shen, J. Chen, H.-L. Yip and S.-J. Su, *Adv. Funct. Mater.*, 2021, **31**, 2106691.

10 (*a*) S. Y. Yang, J. Seidel, S. J. Byrnes, P. Shafer, C. H. Yang, M. D. Rossell, P. Yu, Y. H. Chu, J. F. Scott, J. W. Ager, L. W. Martin and R. Ramesh, *Nat. Nanotechnol.*, 2010, **5**, 143–147; (*b*) Z. Xiao, Y. Yuan, Y. Shao, Q. Wang, Q. Dong,

C. Bi, P. Sharma, A. Gruverman and J. Huang, *Nat. Mater.*, 2015, **14**, 193–198.

11 (*a*) N. Ma and Y. Yang, *Nano Energy*, 2017, **40**, 352–359; (*b*) W. Guo, H. Xu, W. Weng, L. Tang, Y. Ma, Y. Liu, L. Hua, B. Wang, J. Luo and Z. Sun, *Angew. Chem., Int. Ed.*, 2022, **61**, e202213477.

12 L. Guo, X. Liu, L. Gao, X. Wang, L. Zhao, W. Zhang, S. Wang, C. Pan and Z. Yang, *ACS Nano*, 2022, **16**, 1280–1290.

13 (*a*) T. M. H. Nguyen, S. Kim and C. W. Bark, *J. Mater. Chem. A*, 2021, **9**, 1269–1276; (*b*) Z. Yang, H. Wang, L. Guo, Q. Zhou, Y. Gu, F. Li, S. Qiao, C. Pan and S. Wang, *Small*, 2021, **17**, 2101572; (*c*) I.-H. Park, K. C. Kwon, Z. Zhu, X. Wu, R. Li, Q.-H. Xu and K. P. Loh, *J. Am. Chem. Soc.*, 2020, **142**, 18592–18598; (*d*) C. Fang, H. Wang, Z. Shen, H. Shen, S. Wang, J. Ma, J. Wang, H. Luo and D. Li, *ACS Appl. Mater. Interfaces*, 2019, **11**, 8419–8427; (*e*) S. Wang, L. Li, W. Weng, C. Ji, X. Liu, Z. Sun, W. Lin, M. Hong and J. Luo, *J. Am. Chem. Soc.*, 2020, **142**, 55–59.

14 (*a*) X. Cheng, Z. Xie, W. Zheng, R. Li, Z. Deng, D. Tu, X. Shang, J. Xu, Z. Gong, X. Li and X. Chen, *Adv. Sci.*, 2022, **9**, 2103724; (*b*) Y. Ma, W. Guo, Q. Fan, H. Xu, L. Tang, Y. Liu, W. Li, X. Liu, J. Luo and Z. Sun, *Adv. Funct. Mater.*, 2023, **33**, 2210235.

15 X. Li, Y. Wu, S. Zhang, B. Cai, Y. Gu, J. Song and H. Zeng, *Adv. Funct. Mater.*, 2016, **26**, 2435–2445.

16 S. Guo, K. Bu, J. Li, Q. Hu, H. Luo, Y. He, Y. Wu, D. Zhang, Y. Zhao, W. Yang, M. G. Kanatzidis and X. Lü, *J. Am. Chem. Soc.*, 2021, **143**, 2545–2551.